



**HAL**  
open science

## Design of Unipolar Barrier for Nanocrystal Based Short Wave Infrared Photodiode

Amardeep Manikrao Jagtap, Bertille Martinez, Nicolas Goubet, Audrey Chu, Clément Livache, Charlie Gréboval, Julien Ramade, Dylan Amelot, Paul Troussel, Amaury Triboulin, et al.

► **To cite this version:**

Amardeep Manikrao Jagtap, Bertille Martinez, Nicolas Goubet, Audrey Chu, Clément Livache, et al.. Design of Unipolar Barrier for Nanocrystal Based Short Wave Infrared Photodiode. ACS photonics, 2018, 10.1021/acsp Photonics.8b01032 . hal-01908221

**HAL Id: hal-01908221**

**<https://hal.science/hal-01908221>**

Submitted on 10 Jul 2020

**HAL** is a multi-disciplinary open access archive for the deposit and dissemination of scientific research documents, whether they are published or not. The documents may come from teaching and research institutions in France or abroad, or from public or private research centers.

L'archive ouverte pluridisciplinaire **HAL**, est destinée au dépôt et à la diffusion de documents scientifiques de niveau recherche, publiés ou non, émanant des établissements d'enseignement et de recherche français ou étrangers, des laboratoires publics ou privés.

# Design of Unipolar Barrier for Nanocrystal Based Short Wave Infrared Photodiode

Amardeep Jagtap<sup>1</sup>, Bertille Martinez<sup>1,2</sup>, Nicolas Goubet<sup>1,2</sup>, Audrey Chu<sup>1</sup>, Clément Livache<sup>1,2</sup>, Charlie Gréboval<sup>1</sup>, Julien Ramade<sup>1,2</sup>, Dylan Amelot<sup>1</sup>, Paul Troussel<sup>1</sup>, Amaury Triboulin<sup>1</sup>, Sandrine Ithurria<sup>2</sup>, Mathieu G. Silly<sup>3</sup>, Benoit Dubertret<sup>2</sup>, Emmanuel Lhuillier<sup>1\*</sup>

<sup>1</sup> Sorbonne Université, CNRS, Institut des NanoSciences de Paris, INSP, F-75005 Paris, France.

<sup>2</sup> Laboratoire de Physique et d'Étude des Matériaux, ESPCI-Paris, PSL Research University, Sorbonne Université Univ Paris 06, CNRS UMR 8213, 10 rue Vauquelin 75005 Paris, France

<sup>3</sup> Synchrotron-SOLEIL, Saint-Aubin, BP48, F91192 Gif sur Yvette Cedex, France

\* To whom correspondence should be sent: el@insp.upmc.fr

**Abstract:** Nanocrystals are promising materials for the design of low cost infrared detectors. Here we focus on HgTe colloidal quantum dots (CQDs) as an active material for detection in the extended short-wave infrared (2.5  $\mu\text{m}$  as cut-off wavelength). In this paper, we propose a strategy to enhance the performances of previously reported photodiodes. In particular we integrate in this diode an unipolar barrier which role is to prevent the dark current injection to enhance the signal to noise ratio. We demonstrate that such unipolar barrier can be designed from another layer of HgTe CQDs with a wider band gap. Using a combination of IR spectroscopy and photoemission, we show that the barrier is resonant with the absorbing layer valence band, while presenting a clear offset with the conduction band. The combination of contacts with improved design and use of unipolar barrier allows us to reach a detectivity as high as  $3 \cdot 10^8$  Jones at room temperature with 3 dB cut off frequency above 10 kHz.

**Keywords:** nanocrystals, infrared photodetection, short wave infrared, photodiode

## INTRODUCTION

Colloidal nanocrystals are promising materials for the design of low-cost optoelectronic devices. Beyond their bright luminescence properties, which are used in displays and light emitting diodes (LEDs), their use for infrared detection have generated a lot of interest over the recent years<sup>1</sup> especially for two applications: solar cells<sup>2</sup> (*ie* at wavelengths below 1  $\mu\text{m}$ ) and thermal imaging (for wavelengths above 3  $\mu\text{m}$ ).<sup>3</sup>

The intermediate range of wavelengths from 1 to 3  $\mu\text{m}$  is called short wave infrared range (SWIR) and finds applications such as imaging of biological tissue sections,<sup>4,5</sup> telecommunications, night-glow assisted night vision<sup>6</sup> and active imaging.<sup>7</sup> InGaAs is the leading technology in this range of wavelengths. Performances reached by InGaAs detectors are undoubtedly impressive with high quantum efficiency around 80 % and low dark current densities ( $\approx 10^{-9}$  A $\cdot\text{cm}^{-2}$ ). However, InGaAs technology suffers from two main issues, which are its high fabrication cost and the lack of wavelength tunability. In this sense, nanocrystals may offer an interesting low-cost platform especially if they can reach wavelengths where InGaAs is not effective.

Here we typically target the extended SWIR for detection up to 2.5  $\mu\text{m}$  (4000  $\text{cm}^{-1}$  or 0.5 eV). Mercury chalcogenides are certainly the most mature material to achieve absorption and photoconduction in this range of wavelengths. There is nevertheless a limited number of reports based on mercury chalcogenides photodiodes, which are generally focused either on shorter<sup>8,9</sup> or longer wavelengths.<sup>10-12</sup>

Our group has recently reported photodetection at this wavelength (2.5  $\mu\text{m}$ ) using HgTe nanocrystals.<sup>13</sup> In addition to report an encapsulation strategy to obtain stable in air operability, we have also pointed that photodiodes can be an interesting way to enhance the device detectivity, compared to photoconductive devices.<sup>10</sup> The reported level of performances (quantum efficiency below 1% and  $D^* \approx 2 \cdot 10^7$  Jones at room temperature) was however too limited. The proposed diode was relying on a Schottky junction with the following structure: ITO/TiO<sub>2</sub>/HgTe/Au, a scheme of its energetic profile is shown in Figure 1c. This structure was nevertheless suffering from two major flaws: (i) energetically unoptimized contact design, which limited the extraction of photocharged carriers and (ii) a too high dark current, as shown in Figure 1c.

To further enhance the performances of this device, not only we improve the charge extraction by optimizing the contact design, but we propose to introduce an unipolar barrier to reduce the electronic dark current. While the concept of unipolar barrier has been extensively investigated for infrared photodetection based on III-V epitaxially grown semiconductors,<sup>14-16</sup> it has only been marginally applied to colloidal nanocrystal based solar cells to funnel the carriers in a graded band gap structure,<sup>17</sup> or in p-n junctions.<sup>18</sup> Here, we integrate this unipolar barrier to reduce the dark current of our device and increase the detectivity, see Figure 1b and d. We report HgTe nanocrystal-based photodiodes with detectivity reaching  $3 \cdot 10^8$  Jones for 2.5  $\mu\text{m}$  detection at room temperature. This is an order of magnitude larger than the value reported for previous diodes at the same wavelength.

## DISCUSSION

Two families of nanocrystal materials are potentially interesting to achieve absorption in the SWIR: lead and mercury chalcogenides. Lead chalcogenide nanocrystals have been extensively used to harvest the near infrared<sup>2</sup> (from 800 nm to 1  $\mu\text{m}$ ) part of the solar spectrum in quantum dots based solar cells. However, in the extended SWIR (>2.5  $\mu\text{m}$ ), they are difficult to integrate<sup>19,20</sup> into

photodiodes with a vertical geometry. Indeed, large nanoparticles are required to reduce the confinement energy and achieve band edge energy around 0.5 eV, and such nanoparticles tend to have a poor colloidal stability. This leads to CQD films with a low quality (*ie* with pinholes) and results in electrical shortcuts. To build a detector based on CQDs in the extended SWIR, narrower band gap materials are required and mercury chalcogenides compounds offer the most mature alternative.<sup>21-24</sup>

In the following we will focus on HgTe as active material to address the extended SWIR range. HgTe CQDs have been synthesized using the procedure developed by Keuleyan *et al.*<sup>25</sup> Nanoparticles have a tetrapodic shape with a size around 8 nm, see transmission electron microscopy (TEM) image in Figure 1a, and they present an optical band edge at 4000  $\text{cm}^{-1}$  (0.5 eV or 2.5  $\mu\text{m}$ ), see Figure 1a. It was previously demonstrated that the material is an ambipolar conductor (*ie* it conducts both holes and electrons), see supporting information figure S1 and S3-5. Its work function is equal to  $4.7 \pm 0.1$  eV and it presents an Urbach energy, which describes the gap trap distribution, of 35 meV.<sup>13,26</sup>

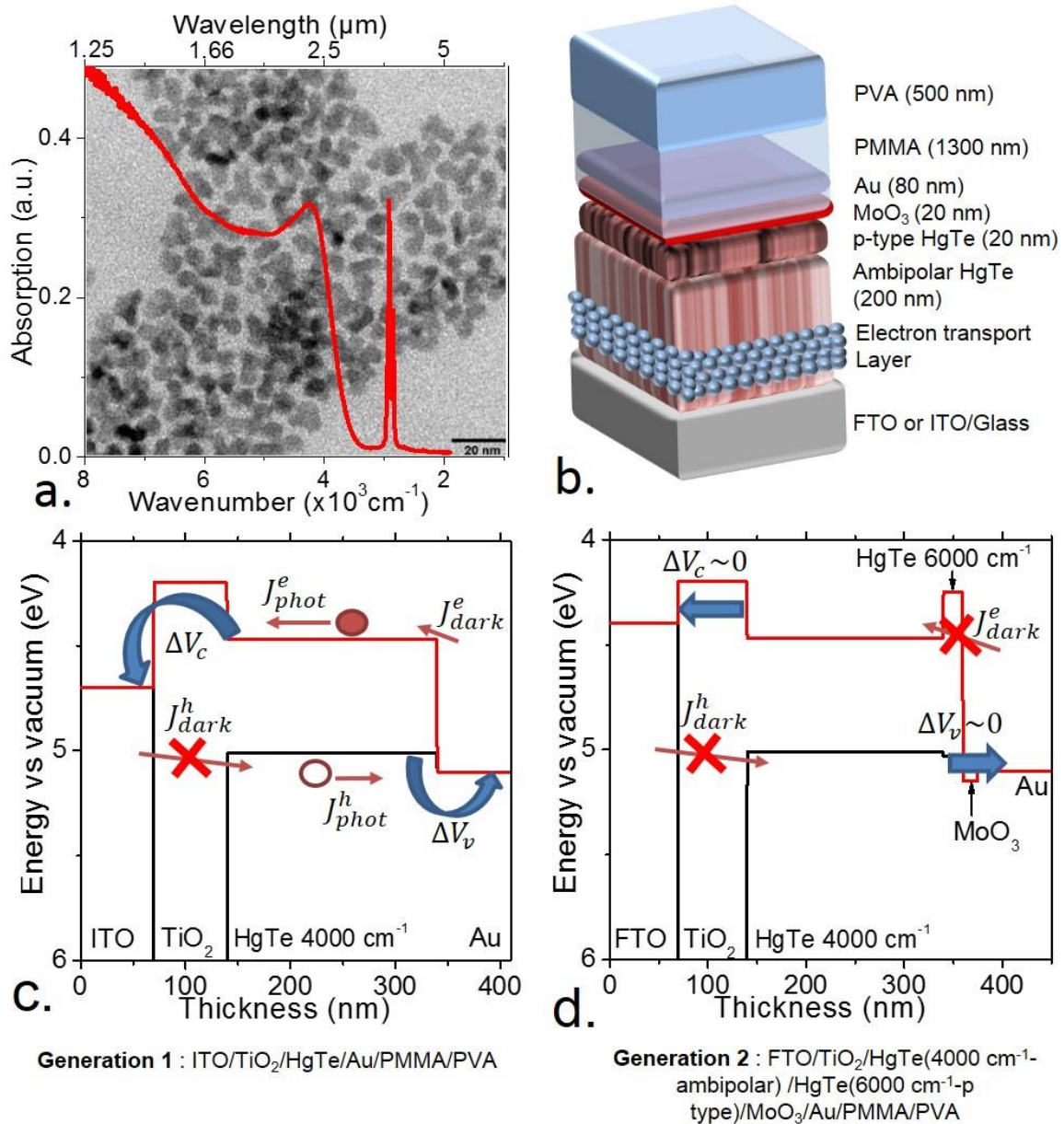


Figure 1 a. Infrared spectrum of HgTe nanocrystals with a band-edge energy at 4000  $\text{cm}^{-1}$ . The background is a TEM image of HgTe nanocrystals. b. Scheme of electrically active photodiode. c. Energy

*band profile of the first generation of short wave infrared photodiode with a structure ITO/TiO<sub>2</sub>/HgTe (ambipolar – 4000 cm<sup>-1</sup>)/Au. d. Energy band profile of the second generation of short wave infrared photodiode with a structure FTO/TiO<sub>2</sub>/HgTe (ambipolar – 4000 cm<sup>-1</sup>)/HgTe (p type – 6000 cm<sup>-1</sup>)/MoO<sub>3</sub>/Au. The relative position of the band is determined assuming a 4.7 eV work function for ITO,<sup>27</sup> 4.4 eV work function for FTO,<sup>28</sup> 5.1 eV for gold and 3.2 eV band gap for anatase TiO<sub>2</sub><sup>29</sup> with HOMO and LUMO respectively at 7.3 eV and 4.1 eV. Band alignment for MoO<sub>3</sub> (figure S1) and values for HgTe (figure S6) are the one determined in the supporting information.*

Jagtap *et al*<sup>13</sup> proposed a first generation of HgTe based photodiode operating in the extended SWIR based on a ITO/TiO<sub>2</sub>/HgTe/Au structure, see Figure 1c. While oxides layers are processed in air, all the following steps of the device fabrication are conducted in air-free conditions to avoid the substantial increase of dark conductance observed when ligand-exchanged HgTe CQD films are exposed to air.<sup>13,30,31</sup> On top of the device, a thick Poly(methyl-methacrylate) (PMMA; water repellent) and Poly(vinyl alcohol) (PVA; O<sub>2</sub> repellent) are deposited at low temperature (room temperature and annealed at 50 °C) to encapsulate and obtain air-stable performances.<sup>13</sup>

The I-V curve rectifying behavior is the result of the TiO<sub>2</sub> layer, which is used as electron extractor and hole blocking layer (see Figure 1c). The responsivity of this structure (a few  $\mu\text{A}\cdot\text{W}^{-1}$  around 0 V) is actually very low, which is the signature of a poor photocharge extraction. Optimizing the electron and hole extraction is required to increase device performances. In the first section of this paper we discuss how both hole and electron extractions can be improved by designing better contacts.

We first screen the effect of adding a hole extraction layer between the HgTe CQD layer and the gold contact. We chose to deposit a MoO<sub>3</sub> layer (a scheme of the device is given in Figure 1b). The effect of this layer on the device responsivity is shown in Figure 2a. In presence of this layer, we observe an increase of the responsivity up to a factor two. The optimal thickness is in the range from 10 to 20 nm, see the inset of Figure 2a.

Similarly, we screen different strategies to prepare the electron extraction layer. Two transparent conductive oxides have been tested (indium tin oxide: ITO and fluorine doped tin oxide: FTO) and two electron transport layers have been tested (ZnO and TiO<sub>2</sub>), see Figure 2b. Out of these four combinations, the combination of FTO and TiO<sub>2</sub> is the one leading to the highest responsivity with a factor two improvement compared to the former generation, see the inset of Figure 2b. This improvement comes from the better band alignment between FTO and the top of the conduction band of TiO<sub>2</sub>, see Figure 1c-d.

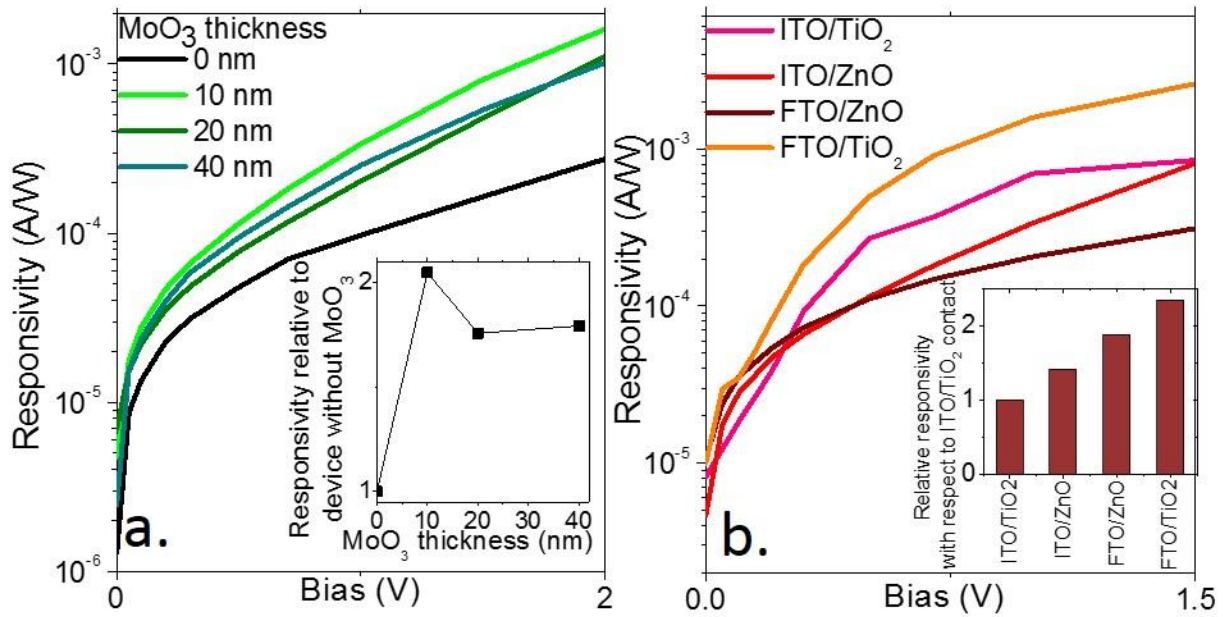


Figure 2 a. Responsivity for a photodiode with the following structure ITO/ZnO/HgTe (ambipolar -4000 cm<sup>-1</sup>)/MoO<sub>3</sub>/Au as a function of the applied bias over the diode for different thicknesses of the MoO<sub>3</sub> layer. The inset plot is the relative evolution of the responsivity as a function of the MoO<sub>3</sub> thickness for a 50 mV bias. b. Responsivity for a photodiode with the following structure of transparent conductive layer/n-type conduction layer/HgTe (ambipolar -4000 cm<sup>-1</sup>)/MoO<sub>3</sub>/Au as a function of the applied bias over the diode for different couples of transparent conductive layer (ITO and FTO) and n-type extraction layer (ZnO and TiO<sub>2</sub>). The thickness of the MoO<sub>3</sub> layer is 10 nm. The inset plot is the relative evolution of the responsivity for the different considered couples of transparent conductive layer and n-type extraction layer, under 50 mV bias.

In the following, we aim to design an unipolar barrier,<sup>14-16</sup> whose role will be to prevent the electron injection from the gold contact, while still letting the photogenerated holes being collected, see Figure 1d. There are three main criteria for the design of such unipolar barrier. (i) First, this unipolar barrier needs to present a wider band gap than the absorbing layer (*ie* above 0.5 eV here). (ii) Secondly, the band alignment needs to be suited to let the photohole flows (*ie* no valence band offset). In other words, the unipolar barrier valence band needs to be aligned with the absorbing layer valence band while the conduction band needs to be offset, by an amount  $\gg k_B T$  where  $k_B$  is Boltzmann constant and  $T$  is the operating temperature. Last, (iii) the barrier must have an unipolar behavior (here p-type is desirable) from a transport point of view.

In the following, we demonstrate that another layer of HgTe with a wider band gap can be used as unipolar barrier. To reach this goal, a first challenge is to identify a strategy to control the majority carrier in a layer of HgTe CQDs.

We have tested the effect of changing the mercury precursor during the synthesis. The procedure developed by Keuleyan is based on HgCl<sub>2</sub>.<sup>25</sup> It was recently demonstrated that other halides may have a huge impact on reaction kinetics and final shape of particles.<sup>32</sup> It was also demonstrated that for the same ligands (S<sup>2-</sup>), mercury chalcogenides might be p-type when the (111) facet is exposed<sup>33</sup> or might even become n-type when the (100) facet is exposed<sup>34</sup>. As a result, we may have speculated that the small change of shape may result in different doping magnitude. However, no such effect has been observed, see figure S3. A second hypothesis to tune the majority carrier is a change in the reaction stoichiometry. It is known that n-type character of II-VI semiconductor CQDs results from their cation-rich surface.<sup>35</sup> As the reaction conditions are changed from a 1:1 Hg/Te ratio to a 50% excess in mercury

or tellurium, no significant change in the Fermi level position or carrier mobility has been observed, see Figure S4.

On the other hand, we determine that the ligand used to quench the reaction is playing a critical role on the nature of the majority carrier, see Figure 3a. Compared to the Keuleyan's procedure<sup>25</sup> for which the synthesis is quenched by adding dodecanethiol and TOP, we now use oleic acid. By doing so, the infrared spectrum presents very limited changes, see Figure 3a and 3c. The change of capping ligands nevertheless comes at the price of a much lower colloidal stability. Indeed, as opposed to thiols, acids are hard bases from Pearson's theory and thus poorly bond to  $\text{Hg}^{2+}$ , which is a soft acid. Then for both initial capping ligands, we conduct a solid-state ligand exchange toward ethanedithiol. Transport properties are conducted in an ion gel quasi solid electrolyte gated transistor configuration.<sup>36–38</sup> This field effect transistor configuration allows (i) air operability of the device, (ii) low operating biases and (iii) gating of thick films. HgTe quenched with dodecanethiol leads to an ambipolar behavior, see Figure 3b, while the oleic acid quenched materials are only p-type, see Figure 3d. We speculate that this difference of behavior is the result of the weak bonding of oleic acid to the CQD surface. As a result, oleic acid ligands are easier to strip from the CQD surface than the DDT molecules. Thus, we have identified a path to control the majority carrier of HgTe CQDs at the synthetic level by tuning the ligand used to quench the reaction.

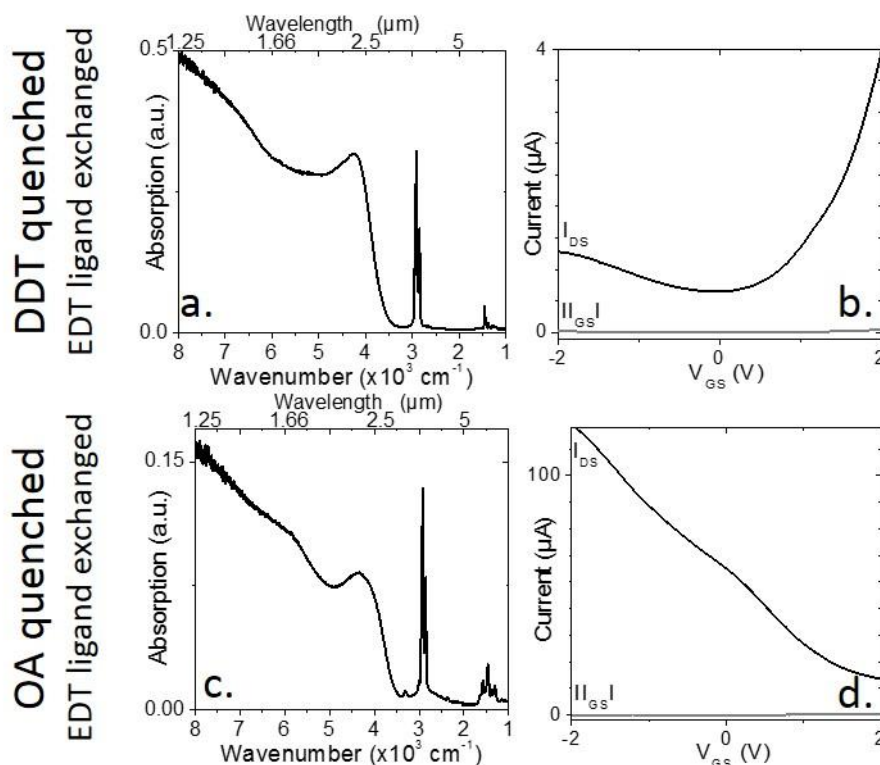


Figure 3 a. Infrared spectrum for dodecanethiol quenched HgTe CQDs with band edge at  $4000 \text{ cm}^{-1}$ . b. Transfer curve (drain current as a function of gate bias) for dodecanethiol quenched HgTe CQDs with band edge at  $4000 \text{ cm}^{-1}$ . c Infrared spectrum for oleic acid quenched HgTe CQDs with band edge at  $4000 \text{ cm}^{-1}$ . d. Transfer curve (drain current as a function of gate bias) for oleic acid quenched HgTe CQDs with band edge at  $4000 \text{ cm}^{-1}$ . Note that for both transistor measurements, the long ligands have been exchanged for ethanedithiol. All transistor curves are acquired at room temperature under a 400 mV bias.

In addition of the surface chemistry effect, we have observed a huge change of transport behavior with the CQD size. Transistor measurements, see Figure 4a-c and figure S5, reveal a switch from p-type to

ambipolar and finally to n-type as the CQD size increases. In particular, materials with band gap larger than  $5500\text{ cm}^{-1}$  ( $0.68\text{ eV}$ ) present only p-type behavior, see Figure 4d. These results are consistent with the reconstructed electronic spectrum of this material probed by photoemission, see Figure 4e and S6. The Fermi level is in the bottom part of the band gap for the widest band gap materials ( $7000\text{ cm}^{-1} \approx 0.87\text{ eV}$  and  $6000\text{ cm}^{-1} \approx 0.75\text{ eV}$  band edge energy); in the upper part of the band gap, but still close to the middle for intermediate band gap ( $4000\text{ cm}^{-1} \approx 0.5\text{ eV}$  and  $2700\text{ cm}^{-1} \approx 0.33\text{ eV}$  band edge energy); while for the smallest band gap, the Fermi level is found to be within the conduction band. This degenerate doping is confirmed by the optical spectrum, see figure S5, on which an intraband feature is appearing.

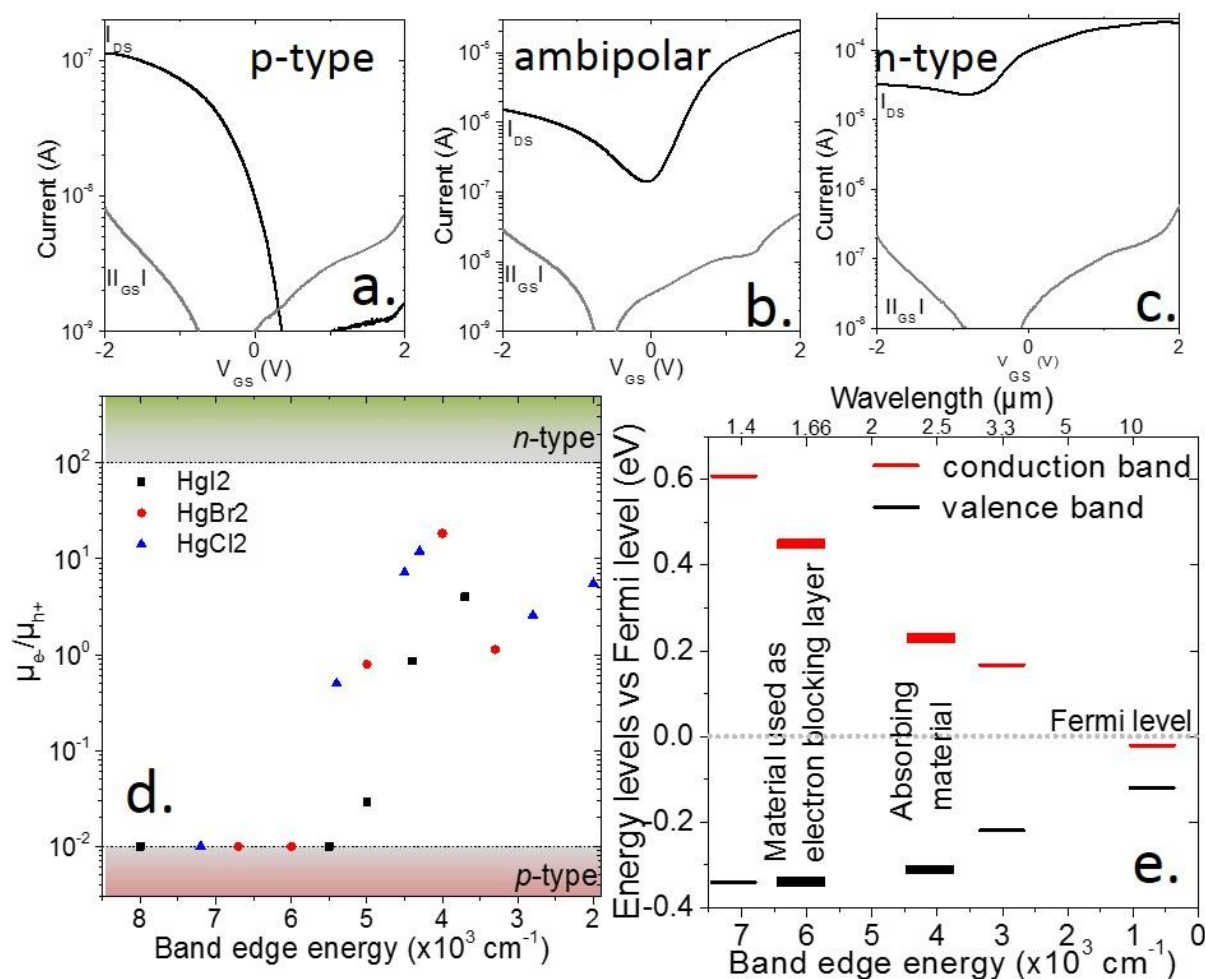


Figure 4 a, b and c are respectively transfer curves for electrolyte gated thin films of HgTe CQDs with band edge at  $7000\text{ cm}^{-1}$ ,  $4000\text{ cm}^{-1}$  and  $700\text{ cm}^{-1}$ . All transistor curves are acquired at room temperature under a  $400\text{ mV}$  bias. d. Ratio of the electron and hole mobilities ( $\mu_e/\mu_{h+}$ ) for thin films of HgTe with different band edges. When material presents only p-type conduction, we set the ratio  $\mu_e/\mu_{h+}$  to  $10^{-2}$ . e. Band alignment of HgTe nanocrystals with different values of band edge energy. In particular, we highlight the weak valence band offset between  $4000\text{ cm}^{-1}$  and  $6000\text{ cm}^{-1}$  band edge energy materials.

To build an unipolar barrier, the band alignment is certainly the most critical aspect. The combination of infrared spectroscopy (to determine the band edge energy) and photoemission spectroscopy (to locate the valence band with respect to the Fermi level) has been used to determine the relative position of HgTe band gap as a function of the nanocrystal size, see Figure 4e. As opposed to what has

been measured with electrochemistry,<sup>39</sup> we observe almost no valence band offset for the smallest size of CQDs. As a result, using a layer of HgTe CQDs with a  $6000\text{ cm}^{-1}$  ( $\approx 0.75\text{ eV}$ ) band edge energy appears as a suitable path for the design of a unipolar barrier. 90 % of the increase of band gap, with respect to the absorbing material band gap, is a conduction band offset, while the valence band offset is typically of the order of  $k_B T$  at room temperature. Moreover, the material has a clear unipolar behavior, conducting only holes. In the next step, we integrate a thin layer of p-type HgTe with a  $6000\text{ cm}^{-1}$  band gap between the absorbing layer and the hole extraction layer made of  $\text{MoO}_3$ .

Thanks to the unipolar barrier based on HgTe CQDs with a  $6000\text{ cm}^{-1}$  band edge, we observe a clear increase of the photoresponse, especially in the low bias range, see Figure 5a. The internal quantum efficiency,  $(\eta_{\text{int}} \%) = \Delta I_{\text{Ph}} / (e\Phi)$ , where  $\Delta I_{\text{Ph}}$  is the photocurrent at 0 V bias,  $e$  is the electronic charge and  $\Phi$  is the photon flux (photon/seconds), is enhanced by  $\approx 26$ -fold as compared to the photovoltaic device without p-type HgTe layer.

The noise of the device has been measured, see figure S10 and is clearly limited by  $1/f$  contribution.<sup>40–42</sup> The addition of the p-type barrier clearly impacts the detectivity, which is increased by an order of magnitude reaching a value of  $3 \cdot 10^8$  Jones at room temperature, see the inset of Figure 5a. To further motivate this study, we compare the progress in terms of responsivity and detectivity between the first and second generations of diodes, see Figure 5b and c. We notice that the fast time response of the first generation has been preserved and show that the 3 dB cut-off frequency is above 10 kHz (actually measurement is setup-limited in this case), see Figure 5d. We provide in table S1 a comparison of the current device performances with other detectors reported in the SWIR range and based on colloidal nanocrystals. The performance of the diode is typically the highest reported for a HgTe CQD based photovoltaic device in the extended SWIR regime. By the time we submit our paper we became aware of even higher performance ( $D^*$  of  $8 \cdot 10^9$  Jones at room temperature) obtained in a photoconductive configuration by the group of Halpert's group,<sup>24</sup> thanks to inorganic capping ligands.

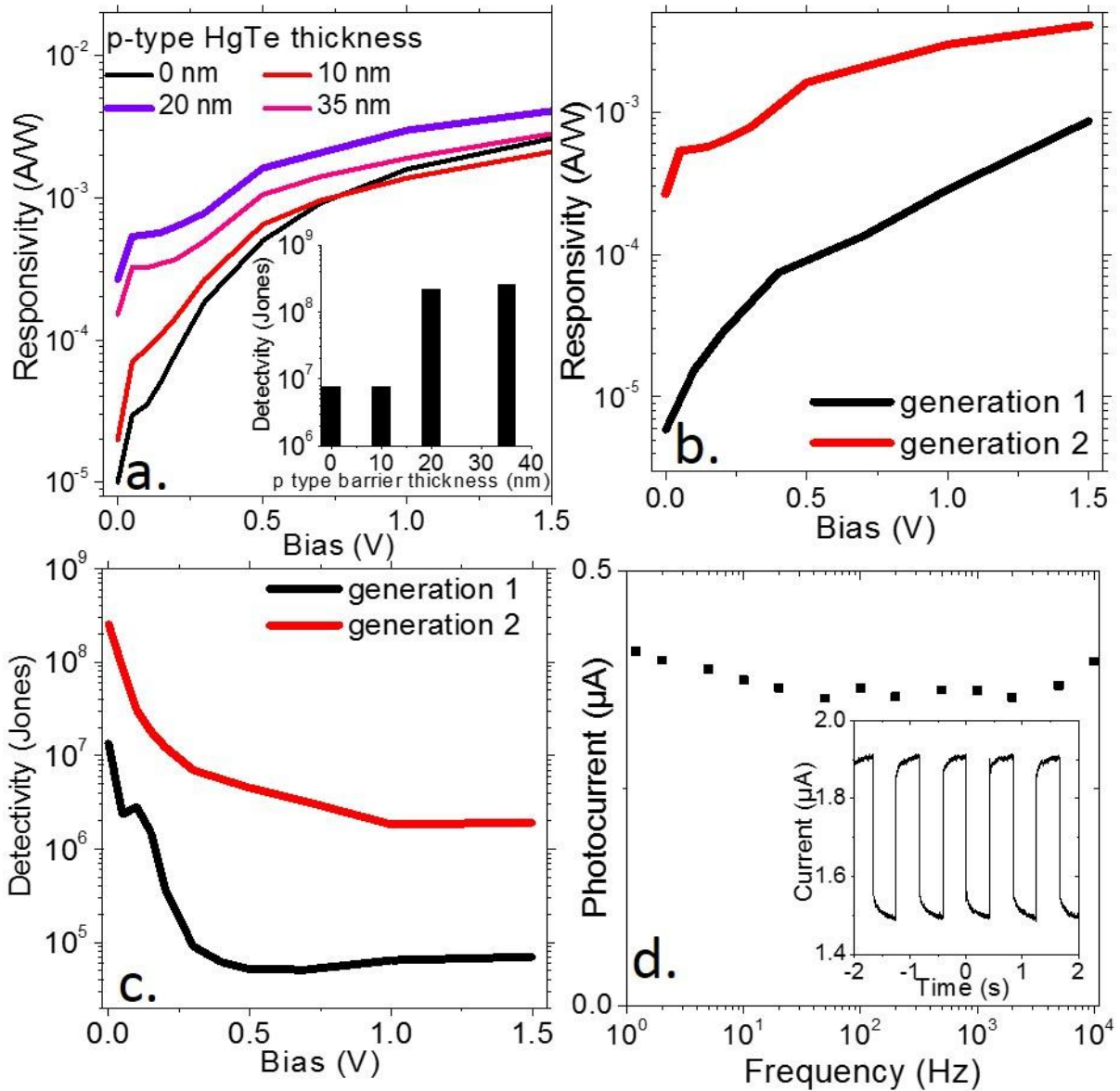


Figure 5 a. Responsivity as a function of the applied bias for different thicknesses of the HgTe  $6000 \text{ cm}^{-1}$  p-type layer used as electron blocking layer for a FTO/TiO<sub>2</sub>/HgTe (ambipolar -  $4000 \text{ cm}^{-1}$ )/HgTe (p-type -  $6000 \text{ cm}^{-1}$ )/MoO<sub>3</sub>/Au photodiode. The inset reports the detectivity value of this diode, at 0 V and room temperature, for different thicknesses of the HgTe  $6000 \text{ cm}^{-1}$  p-type layer used as electron blocking layer. b. Responsivity as a function of the applied bias for ITO/TiO<sub>2</sub>/HgTe (ambipolar -  $4000 \text{ cm}^{-1}$ )/Au and for FTO/TiO<sub>2</sub>/HgTe (ambipolar -  $4000 \text{ cm}^{-1}$ )/HgTe (p-type -  $6000 \text{ cm}^{-1}$ )/MoO<sub>3</sub>/Au photodiode. c. Detectivity as a function of the applied bias for ITO/TiO<sub>2</sub>/HgTe (ambipolar -  $4000 \text{ cm}^{-1}$ )/Au and for FTO/TiO<sub>2</sub>/HgTe (ambipolar -  $4000 \text{ cm}^{-1}$ )/HgTe (p-type -  $6000 \text{ cm}^{-1}$ )/MoO<sub>3</sub>/Au photodiode. d Bode diagram for the device of the second generation giving the frequency dependence of the photocurrent. The inset is a time trace of the photocurrent as the light source (here a  $1.55 \mu\text{m}$  laser diode) is turned on and off.

## CONCLUSION

We develop a strategy to design an unipolar barrier to filter the electron dark current while letting the photo-holes flow in HgTe nanocrystals based photodiode. To do so, we develop a method to control

the majority carrier in HgTe CQD films based on the choice of the quenching ligand during the synthesis. We also demonstrate that size strongly drives the nature of the majority carriers from holes for small particles to electrons for large HgTe CQDs. Combination of transport and photoemission measurements is used to demonstrate that a layer of HgTe CQDs with a band edge energy at  $6000\text{ cm}^{-1}$  actually fits with criteria for the design of unipolar barrier with almost no valence band offset but a  $>200\text{ meV}$  barrier in the conduction band. The addition of this layer is used to enhance the responsivity and detectivity of the device. The latter now reaches  $3 \cdot 10^8$  Jones at room temperature with 3 dB cut-off frequency above 10 kHz.

## METHODS

### Nanocrystal synthesis

**1 M TOP:Te precursor:** 2.54 g of Te powder is mixed in 20 mL of TOP in a three neck flask. The flask is kept under vacuum at room temperature for 5 min and then the temperature is raised to  $100\text{ }^\circ\text{C}$ . Furthermore, degassing of flask is conducted for the next 20 min. The atmosphere is switched to Ar and the temperature is raised to  $275\text{ }^\circ\text{C}$ . The solution is stirred until a clear orange coloration is obtained. The flask is cooled down to room temperature and the color switches to yellow. Finally, this solution is transferred to an Ar filled glove box for storage.

**HgTe CQD synthesis with band edge at  $4000\text{ cm}^{-1}$ :** In a 100 mL three-neck flask, 513 mg of  $\text{HgCl}_2$  and 60 mL of oleylamine are degassed at  $110\text{ }^\circ\text{C}$  for 1 h. Under Ar at  $80\text{ }^\circ\text{C}$ , a solution containing 1.9 mL of 1 M TOP:Te and 10 mL of oleylamine is quickly injected after warming it up with heat gun. After 3 min, the reaction is quickly quenched by adding a mixture of toluene (9 mL) and dodecanethiol (1 mL), the flask is then cooled down using air flux. The nanocrystals are precipitated in ethanol and redispersed in toluene. This washing is repeated one more time. Finally, the HgTe CQDs dispersed in toluene are filtered through a  $0.2\text{ }\mu\text{m}$  PTFE filter. The obtained solution is used for further characterizations and fabrication of devices. Synthesis of HgTe nanocrystals with other sizes are discussed in the supporting information.

**ITO patterning:** ITO substrates are cut into  $15 \times 15\text{ mm}$  size and thoroughly cleaned by sonication in acetone for 5 min, rinsed with acetone and isopropanol, then dried completely with dry  $\text{N}_2$  flow. AZ 5214E photoresist is spin-coated for 30 s and subsequently the substrates are baked at  $110\text{ }^\circ\text{C}$  for 90 s. At next stage, standard photolithography is performed using mask aligner for exposing the substrates to UV light for 5 s through a lithography mask (1 mm width). Photoresist is developed using AZ 726 developer for 40 s and immediately rinsed with de-ionized water. Thus, exposed ITO surface is completely etched out with 25 % HCl (in water) for 12 min and substrates are dipped immediately in de-ionized water. Then, lift-off is conducted in an acetone bath and patterned ITO substrates are cleaned with acetone and isopropanol. Finally, substrates are dried with dry  $\text{N}_2$  flow.

**FTO patterning:** FTO substrates are cut into  $15 \times 15\text{ mm}$  size and thoroughly cleaned by sonication in acetone bath for 5 min, rinsed with acetone and isopropyl alcohol and finally dried completely with dry  $\text{N}_2$  flow. Photoresist (AZ 5214E) is spin-coated for 30 s and subsequently the substrates are baked at  $110\text{ }^\circ\text{C}$  for 90 s. At next stage, photolithography is performed using mask aligner for exposing the substrates to UV light for 5 s through a lithography mask (1 mm width). AZ 726 developer is used for developing the pattern in 40 s and immediately rinsed with de-ionized water. Afterwards, Zn powder is sprinkled on developed substrates and excess Zn powder is removed from substrates. This process is

repeated twice. Thus, exposed FTO surface is completely etched out with 2 M HCl (2 mL of 37 % HCl in 10 mL of DI water) for 15 min and cotton knob is used to remove any remaining Zn powder from substrate surface. At next stage, substrates are dipped immediately in de-ionized water. Then, lift-off is carried out in an acetone bath and patterned FTO substrates are thoroughly cleaned with acetone and isopropyl alcohol. Finally, substrates are dried with dry N<sub>2</sub> flow.

**TiO<sub>2</sub> and ZnO film preparation:** 200 µL of anatase TiO<sub>2</sub> nanoparticle solution is spin-coated on above patterned ITO and FTO substrates at 5000 rpm for 30 s. The TiO<sub>2</sub> film is annealed at 200 °C for 15 min and its thickness is measured to be 65 nm with Dektak profilometer. ZnO nanocrystal film is obtained by spin coating ZnO nanocrystals at 3000 rpm for 45 s and annealing the film at 250 °C for 30 min. This process is repeated one more time to build a 200 nm thick layer

**HgTe nanocrystal film preparation and EDT ligand exchange in air free conditions:** Film preparation and ligand exchange processes are carried out inside a N<sub>2</sub> filled glovebox. In a typical procedure, 80 µL of concentrated HgTe nanocrystals (25 mg/mL) from toluene is spin coated at 2000 rpm for 30 s on above fabricated Glass/ITO/TiO<sub>2</sub> substrates. After complete evaporation of solvent, ligand exchange is carried out by dipping the film in 1 - 2 wt % EDT solution in ethanol for 90 s and rinsing it in pure ethanol for 30 s. Afterwards, a quick annealing step at 50 °C, for 1 min is carried out. This procedure is repeated for 8 – 9 times to get thicker (180 – 200 nm) and pin-hole free HgTe nanocrystal film. Same procedure is followed for ITO/ZnO, FTO/TiO<sub>2</sub> and FTO/ZnO.

**MoO<sub>3</sub>/Au electrode deposition in air free conditions:** Fabricated Glass/ITO/TiO<sub>2</sub>/HgTe substrates are transferred from glove box to the thermal evaporator chamber under N<sub>2</sub> environment. If MoO<sub>3</sub> is included in the device, it is thermally evaporated through a shadow mask (1 mm width) from MoO<sub>3</sub> powder at a rate of  $\approx 1 - 2 \text{ \AA}\cdot\text{s}^{-1}$ . Then 80 nm of Au is thermally evaporated at a rate of  $2 - 3 \text{ \AA}\cdot\text{s}^{-1}$  through the same shadow mask. The latter is aligned to get a pixel of  $1 \times 1 \text{ mm}^2$  area.

**Protective layer of PMMA/PVA:** Above fabricated devices are transferred from thermal evaporator to glovebox under N<sub>2</sub> environment. PMMA (5 wt % in CHCl<sub>3</sub>) solution is spin-coated on substrates at 2000 rpm for 60 s, then a quick annealing step at 50 °C for 1 min is performed. In following steps, PVA (centrifuged solution at 10 wt % in water) is spin coated at 4000 rpm for 60 s. After this step, substrates are annealed for 1 min at 50 °C. Finally, device is kept in vacuum overnight for the complete drying of encapsulation layers. Thus, obtained thicknesses for these encapsulation films are found to be 1.3 µm and 0.5 µm for PMMA and PVA, respectively.

**Responsivity measurements:** The sample is biased using a DC bias from Zurich instrument MFLI lock-in amplifier. The light from a blackbody source at 927 °C is used as broadband infrared source. A Ge filter is used to cut the light at wavelength below 1.8 µm. This light is then chopped using a mechanical chopper. This chopper is used as reference frequency for the lock-in. Photocurrent signal is finally acquired on the lock-in while the chopping frequency is tuned. Figure 5d shows the frequency dependence of the photosignal showing a 3 dB cut-off frequency above 10k Hz. In this case the signal device is illuminated by a laser at 1.55 µm, which input is electrically modulated with a signal generator.

**Noise measurements:** The sample is biased using the input of a Femto DLPCA 200 amplifier. The current through the sample is then amplified using the same current amplifier. The current spectral density is then acquired using a low frequency spectrum analyzer SR 780 from Stanford Research system.

## ACKNOWLEDGMENTS

EL thanks the support ERC starting grant blackQD (grant n° 756225). We acknowledge the use of clean-room facilities from the “Centrale de Proximité Paris-Centre”. This work has been supported by the Region Ile-de-France in the framework of DIM Nano-K (grant dopQD). This work was supported by French state funds managed by the ANR within the Investissements d'Avenir programme under reference ANR-11-IDEX-0004-02, and more specifically within the framework of the Cluster of Excellence MATISSE and also by the grant Nanodose and H2DH. NG, AJ and JR thank Nexdot for post doc funding.

## ASSOCIATED CONTENTS

### Supporting information

The Supporting Information is available free of charge on the ACS Publications website at DOI:

Nanocrystals synthesis for various size, material characterization, transport measurement; effect of halide, stoichiometry and size on doping, noise measurement and comparison with state of the art device in the SWIR range

## REFERENCES

- (1) Kershaw, S. V.; Susha, A. S.; Rogach, A. L. Narrow Bandgap Colloidal Metal Chalcogenide Quantum Dots: Synthetic Methods, Heterostructures, Assemblies, Electronic and Infrared Optical Properties. *Chem. Soc. Rev.* **2013**, *42* (7), 3033–3087.
- (2) Sargent, E. H. Solar Cells, Photodetectors, and Optical Sources from Infrared Colloidal Quantum Dots. *Adv. Mater.* **20** (20), 3958–3964.
- (3) Keuleyan, S.; Lhuillier, E.; Brajuskovic, V.; Guyot-Sionnest, P. Mid-Infrared HgTe Colloidal Quantum Dot Photodetectors. *Nat. Photonics* **2011**, *5* (8), 489–493.
- (4) Thimsen, E.; Sadtler, B.; Berezin, M. Y. Shortwave-Infrared (SWIR) Emitters for Biological Imaging: A Review of Challenges and Opportunities. *Nanophotonics* **2017**, *6* (5), 1043–1054.
- (5) Bruns, O. T.; Bischof, T. S.; Harris, D. K.; Franke, D.; Shi, Y.; Riedemann, L.; Bartelt, A.; Jaworski, F. B.; Carr, J. A.; Rowlands, C. J.; et al. Next-Generation *in Vivo* Optical Imaging with Short-Wave Infrared Quantum Dots. *Nat. Biomed. Eng.* **2017**, *1* (4), 0056.
- (6) Hansen, M. P.; Malchow, D. S. Overview of SWIR Detectors, Cameras, and Applications. In *Thermosense XXX*; International Society for Optics and Photonics, 2008; Vol. 6939, p 69390I.
- (7) Demiguel, S. Theoretical Analysis and Comparison of SWIR Active Imaging Detectors. In *Infrared Technology and Applications XXXV*; International Society for Optics and Photonics, 2009; Vol. 7298, p 729836.
- (8) Chen, M.; Shao, L.; Kershaw, S. V.; Yu, H.; Wang, J.; Rogach, A. L.; Zhao, N. Photocurrent Enhancement of HgTe Quantum Dot Photodiodes by Plasmonic Gold Nanorod Structures. *ACS Nano* **2014**, *8* (8), 8208–8216.
- (9) Nam, M.; Kim, S.; Kim, S.; Jeong, S.; Kim, S.-W.; Lee, K. Near-Infrared-Sensitive Bulk Heterojunction Solar Cells Using Nanostructured Hybrid Composites of HgTe Quantum Dots and a Low-Bandgap Polymer. *Sol. Energy Mater. Sol. Cells* **2014**, *126*, 163–169.
- (10) Guyot-Sionnest, P.; Roberts, J. A. Background Limited Mid-Infrared Photodetection with Photovoltaic HgTe Colloidal Quantum Dots. *Appl. Phys. Lett.* **2015**, *107* (25), 253104.
- (11) Tang, X.; Ackerman, M. M.; Guyot-Sionnest, P. Thermal Imaging with Plasmon Resonance Enhanced HgTe Colloidal Quantum Dot Photovoltaic Devices. *ACS Nano* **2018**, *12* (7), 7362–7370.
- (12) Ackerman, M. M.; Tang, X.; Guyot-Sionnest, P. Fast and Sensitive Colloidal Quantum Dot Mid-Wave Infrared Photodetectors. *ACS Nano* **2018**, *12* (7), 7264–7271.

- (13) Jagtap, A.; Goubet, N.; Livache, C.; Chu, A.; Martinez, B.; Greboval, C.; Qu, J.; Dandeu, E.; Becerra, L.; Witkowski, N.; et al. Short Wave Infrared Devices Based on HgTe Nanocrystals with Air Stable Performances. *J. Phys. Chem. C* **2018**, *122* (26), 14979–14985.
- (14) Martyniuk, P.; Kopytko, M.; Rogalski, A. Barrier Infrared Detectors. *Opto-Electron. Rev.* **2014**, *22* (2), 127–146.
- (15) Savich, G. R.; Pedrazzani, J. R.; Sidor, D. E.; Maimon, S.; Wicks, G. W. Dark Current Filtering in Unipolar Barrier Infrared Detectors. *Appl. Phys. Lett.* **2011**, *99* (12), 121112.
- (16) Savich, G. R.; Pedrazzani, J. R.; Sidor, D. E.; Wicks, G. W. Benefits and Limitations of Unipolar Barriers in Infrared Photodetectors. *Infrared Phys. Technol.* **2013**, *59*, 152–155.
- (17) Kramer, I. J.; Levina, L.; Debnath, R.; Zhitomirsky, D.; Sargent, E. H. Solar Cells Using Quantum Funnel. *Nano Lett.* **2011**, *11* (9), 3701–3706.
- (18) Chuang, C.-H. M.; Brown, P. R.; Bulović, V.; Bawendi, M. G. Improved Performance and Stability in Quantum Dot Solar Cells through Band Alignment Engineering. *Nat. Mater.* **2014**, *13* (8), 796–801.
- (19) Pietryga, J. M.; Schaller, R. D.; Werder, D.; Stewart, M. H.; Klimov, V. I.; Hollingsworth, J. A. Pushing the Band Gap Envelope: Mid-Infrared Emitting Colloidal PbSe Quantum Dots. *J. Am. Chem. Soc.* **2004**, *126* (38), 11752–11753.
- (20) Konstantatos, G.; Howard, I.; Fischer, A.; Hoogland, S.; Clifford, J.; Klem, E.; Levina, L.; Sargent, E. H. Ultrasensitive Solution-Cast Quantum Dot Photodetectors. *Nature* **2006**, *442*, 180–183.
- (21) Green, M.; Mirzai, H. Synthetic Routes to Mercury Chalcogenide Quantum Dots. *J. Mater. Chem. C* **2018**, *6* (19), 5097–5112.
- (22) Lhuillier, E.; Guyot-Sionnest, P. Recent Progresses in Mid Infrared Nanocrystal Based Optoelectronics. *IEEE J. Sel. Top. Quantum Electron.* **2017**, *23*, 6000208.
- (23) Huo, N.; Gupta, S.; Konstantatos, G. MoS<sub>2</sub>-HgTe Quantum Dot Hybrid Photodetectors beyond 2 μm. *Adv. Mater.* **2017**, *29* (17), 1606576.
- (24) Cryer, M. E.; Halpert, J. E. 300 Nm Spectral Resolution in the Mid-Infrared with Robust, High Responsivity Flexible Colloidal Quantum Dot Devices at Room Temperature. *ACS Photonics* **2018**, *5* (8), 3009–3015.
- (25) Keuleyan, S.; Lhuillier, E.; Guyot-Sionnest, P. Synthesis of Colloidal HgTe Quantum Dots for Narrow Mid-IR Emission and Detection. *J. Am. Chem. Soc.* **2011**, *133* (41), 16422–16424.
- (26) Martinez, B.; Livache, C.; Goubet, N.; Jagtap, A.; Cruguel, H.; Ouerghi, A.; Lacaze, E.; Silly, M. G.; Lhuillier, E. Probing Charge Carrier Dynamics to Unveil the Role of Surface Ligands in HgTe Narrow Band Gap Nanocrystals. *J. Phys. Chem. C* **2018**, *122* (1), 859–865.
- (27) Park, Y.; Choong, V.; Gao, Y.; Hsieh, B. R.; Tang, C. W. Work Function of Indium Tin Oxide Transparent Conductor Measured by Photoelectron Spectroscopy. *Appl. Phys. Lett.* **1996**, *68* (19), 2699–2701.
- (28) Qiao, Q.; McLeskey, J. T. Water-Soluble Polythiophene/nanocrystalline TiO<sub>2</sub> Solar Cells. *Appl. Phys. Lett.* **2005**, *86* (15), 153501.
- (29) Ola, O.; Maroto-Valer, M. M. Review of Material Design and Reactor Engineering on TiO<sub>2</sub> Photocatalysis for CO<sub>2</sub> Reduction. *J. Photochem. Photobiol. C Photochem. Rev.* **2005**, *24*, 16–42.
- (30) Chen, M.; Yu, H.; Kershaw, S. V.; Xu, H.; Gupta, S.; Hetsch, F.; Rogach, A. L.; Zhao, N. Fast, Air-Stable Infrared Photodetectors Based on Spray-Deposited Aqueous HgTe Quantum Dots. *Adv. Funct. Mater.* **2013**, *24* (1), 53–59.
- (31) Lhuillier, E.; Keuleyan, S.; Zolotavin, P.; Guyot-Sionnest, P. Mid-Infrared HgTe/As<sub>2</sub>S<sub>3</sub> Field Effect Transistors and Photodetectors. *Adv. Mater.* **2013**, *25* (1), 137–141.
- (32) Goubet, N.; Jagtap, A.; Livache, C.; Martinez, B.; Portalès, H.; Xu, X. Z.; Lobo, R. P. S. M.; Dubertret, B.; Lhuillier, E. Terahertz HgTe Nanocrystals: Beyond Confinement. *J. Am. Chem. Soc.* **2018**, *140* (15), 5033–5036.
- (33) Martinez, B.; Livache, C.; Notemgnou Mouafo, L. D.; Goubet, N.; Keuleyan, S.; Cruguel, H.; Ithurria, S.; Aubin, H.; Ouerghi, A.; Doudin, B.; et al. HgSe Self-Doped Nanocrystals as a Platform to Investigate the Effects of Vanishing Confinement. *ACS Appl. Mater. Interfaces* **2017**, *9* (41), 36173–36180.

- (34) Livache, C.; Izquierdo, E.; Martinez, B.; Dufour, M.; Pierucci, D.; Keuleyan, S.; Cruguel, H.; Becerra, L.; Fave, J. L.; Aubin, H.; et al. Charge Dynamics and Optoelectronic Properties in HgTe Colloidal Quantum Wells. *Nano Lett.* **2017**, *17* (7), 4067–4074.
- (35) Jeong, K. S.; Deng, Z.; Keuleyan, S.; Liu, H.; Guyot-Sionnest, P. Air-Stable n-Doped Colloidal HgS Quantum Dots. *J. Phys. Chem. Lett.* **2014**, *5* (7), 1139–1143.
- (36) Kang, M. S.; Lee, J.; Norris, D. J.; Frisbie, C. D. High Carrier Densities Achieved at Low Voltages in Ambipolar PbSe Nanocrystal Thin-Film Transistors. *Nano Lett.* **2009**, *9* (11), 3848–3852.
- (37) Bisri, S. Z.; Piliago, C.; Yarema, M.; Heiss, W.; Loi, M. A. Low Driving Voltage and High Mobility Ambipolar Field-Effect Transistors with PbS Colloidal Nanocrystals. *Adv. Mater.* **2013**, *25* (31), 4309–4314.
- (38) Lhuillier, E.; Ithurria, S.; Descamps-Mandine, A.; Douillard, T.; Castaing, R.; Xu, X. Z.; Taberna, P.-L.; Simon, P.; Aubin, H.; Dubertret, B. Investigating the N- and p-Type Electrolytic Charging of Colloidal Nanoplatelets. *J. Phys. Chem. C* **2015**, *119* (38), 21795–21799.
- (39) Chen, M.; Guyot-Sionnest, P. Reversible Electrochemistry of Mercury Chalcogenide Colloidal Quantum Dot Films. *ACS Nano* **2017**, *11* (4), 4165–4173.
- (40) Lai, Y.; Li, H.; Kim, D. K.; Diroll, B. T.; Murray, C. B.; Kagan, C. R. Low-Frequency (1/f) Noise in Nanocrystal Field-Effect Transistors. *ACS Nano* **2014**, *8* (9), 9664–9672.
- (41) De Iacovo, A.; Venettacci, C.; Colace, L.; Scopa, L.; Foglia, S. Noise Performance of PbS Colloidal Quantum Dot Photodetectors. *Appl. Phys. Lett.* **2017**, *111* (21), 211104.
- (42) Liu, H.; Lhuillier, E.; Guyot-Sionnest, P. 1/f Noise in Semiconductor and Metal Nanocrystal Solids. *J. Appl. Phys.* **2014**, *115* (15), 154309.

### TOC graphic

